Journal of Alzheimer's Disease 34 (2013) 995–1013
DOI 10.3233/JAD-122038
IOS Press

FIB/SEM Technology and Alzheimer's Disease: Three-Dimensional Analysis of Human Cortical Synapses

Lidia Blazquez-Llorca[a,b], Ángel Merchán-Pérez[a,c], José-Rodrigo Rodríguez[a,b], Jorge Gascón[d] and Javier DeFelipe[a,b,e,*]

[a]*Laboratorio Cajal de Circuitos Corticales (CTB), Universidad Politécnica de Madrid, Campus Montegancedo S/N, Pozuelo de Alarcón, Spain*
[b]*Instituto Cajal (CSIC), Madrid, Spain*
[c]*DATSI, Universidad Politécnica de Madrid, Campus Montegancedo S/N, Pozuelo de Alarcón, Madrid, Spain*
[d]*Universidad Rey Juan Carlos, campus de Móstoles, Móstoles, Spain*
[e]*Centro de Investigación Biomédica en Red sobre Enfermedades Neurodegenerativas (CIBERNED), Spain*

Accepted 21 December 2012

Abstract. The quantification and measurement of synapses is a major goal in the study of brain organization in both health and disease. Serial section electron microscopy (EM) is the ideal method since it permits the direct quantification of crucial features such as the number of synapses per unit volume or the distribution and size of synapses. However, a major limitation is that obtaining long series of ultrathin sections is extremely time-consuming and difficult. Consequently, quantitative EM studies are scarce and the most common method employed to estimate synaptic density in the human brain is indirect, by counting at the light microscopic level immunoreactive puncta using synaptic markers. The recent development of automatic EM methods in experimental animals, such as the combination of focused ion beam milling and scanning electron microscopy (FIB/SEM), are opening new avenues. Here we explored the utility of FIB/SEM to examine the cerebral cortex of Alzheimer's disease patients. We found that FIB/SEM is an excellent tool to study in detail the ultrastructure and alterations of the synaptic organization of the human brain. Using this technology, it is possible to reconstruct different types of plaques and the surrounding neuropil to find new aspects of the pathological process associated with the disease, namely; to count the exact number and types of synapses in different regions of the plaques, to study the spatial distribution of synapses, and to analyze the morphology and nature of the various types of dystrophic neurites and amyloid deposits.

Keywords: Amyloid-β plaques, asymmetric synapses, autopsy material, automatic electron microscopy, cerebral cortex, dystrophic neurites, symmetric synapses, ultrastructure

Supplementary data available online: http://dx.doi.org/10.3233/JAD-122038

INTRODUCTION

Alzheimer's disease (AD) is the most common age-related neurodegenerative disorder and is characterized by two hallmark lesions: extracellular amyloid plaques, primarily consisting of amyloid-β (Aβ) peptide, and intracellular neurofibrillary tangles, which consist of filamentous aggregates of hyperphosphorylated tau protein (e.g., [1]). There is a growing

*Correspondence to: Javier DeFelipe, Laboratorio Cajal de Circuitos Corticales, Centro de Tecnología Biomédica, Universidad Politécnica de Madrid, Campus Montegancedo S/N, Pozuelo de Alarcón, 28223 Madrid, Spain; and Instituto Cajal (CSIC), Avenida Doctor Arce 37, 28002 Madrid, Spain. Tel.: +34 91 336 4639; E-mail: defelipe@cajal.csic.es.

ISSN 1387-2877/13/$27.50

consensus, based primarily on cell-based assays, that Aβ, the main component of senile plaques, is toxic to synapses [2–4]. In both AD patients and animal models of the disease, synapse loss is greatest near Aβ plaques, suggesting a link between Aβ pathology and synaptotoxicity *in vivo* [5]. In addition, numerous studies have reported widespread synaptic dysfunction or loss even in early stages of the disease, and at present it is widely accepted that synapse loss is the major structural correlate of cognitive dysfunction [6–12]. Therefore, elucidation of the changes that affect synapses is crucial for better understanding the pathogenic mechanisms underlying AD.

The gold standard for quantification and measurement of synapses is electron microscopy (EM). However, the classical methods for quantification of synapses with transmission EM (TEM), even using stereological estimates, have significant technical limitations [13]. In addition, the ultrastructural preservation of postmortem human brain tissue is often rather poor, while the ultrastructure of biopsy material is excellent (e.g., [14–26]) and can be studied by accurate correlative light/EM and quantitative EM methods comparable to those performed with experimental animals (e.g., [27–29]), although the amount of tissue removed with biopsy is, for obvious reasons, rather small. For these reasons, quantitative TEM studies are scarce in humans [30–36] and, at present, one of the most common methods employed to estimate synaptic density is indirect, for example by counting synaptophysin-immunoreactive puncta (or other synaptic markers) using conventional light microscopy or confocal microscopy (e.g., [8, 12, 37–40]; for a review, see [6]).

An additional drawback is the need to perform serial reconstructions from ultrathin sections, which is necessary when the final goal is to examine 3D characteristics, such as the number of synapses per unit volume or the distribution and size of synapses. Although serial sectioning TEM is a well-established technique to obtain 3D data of brain tissue (e.g., [41, 42]), a major limitation is that obtaining long series of ultrathin sections is extremely time-consuming and difficult, often making it impossible to reconstruct large volumes of tissue. As a consequence, these EM methods are not widely used in spite of the importance of the information obtained. Indeed, there are very few 3D ultrastructural studies dealing with AD and these have been performed in experimental animals to reconstruct microglia around Aβ plaques in AβPP23 transgenic mice [43], to elucidate the spatial relationship between Aβ deposits and cellular components in 3xTg-AD mice and aged dogs [44], or to reconstruct dystrophic neurites of senile plaques in aged monkeys [45]. However, as far as we know, no detailed 3D studies have been performed to study the cerebral cortex of AD patients.

In recent years, the development of automatic EM methods has been opening new avenues that are expected to soon constitute an essential technology for 3D reconstructions at the ultrastructural level [46]. Indeed, the combination of focused ion beam milling and scanning electron microscopy (FIB/SEM) has proved to be very useful in experimental animals as it not only allows images with a quality and resolution similar to those obtained with TEM, but also has the great advantage of permitting the rapid and automatic serial section of large tissue volumes [47] that can later be reconstructed in 3D with the help of software tools [48]. Therefore, in the present study we explored the utility of FIB/SEM to examine the cerebral cortex of AD patients obtained at autopsy, by far the most common source of human tissue for research. More specifically, we analyzed different regions of Aβ plaques in order to check the validity of this technology to quantify the number and distribution of synapses and to reconstruct some of the abnormal structures that constitute the plaques, such as dystrophic neurites and Aβ deposits. We show that FIB/SEM is an excellent tool to examine alterations of synapses that are in contact Aβ plaques and to obtain 3D reconstructions of the components of the plaques. Furthermore, since the quality of the images was in general strikingly good and better than that obtained with TEM, FIB/SEM is a particularly useful technology to study the human cerebral cortex in both health and disease.

MATERIALS AND METHODS

Human brain tissue from 5 patients with AD (aged 80–94, average 86.4) was obtained from the Instituto de Neuropatología (Dr. I. Ferrer, Servicio de Anatomía Patológica, IDIBELL-Hospital Universitario de Bellvitge, Barcelona, Spain) and from the Banco de Tejidos Fundación CIEN (Dr. A. Rábano, Área de Neuropatología, Centro Alzheimer, Fundación Reina Sofía, Madrid, Spain) (Table 1).

Following neuropathological examination, the pathological state and stage was defined according to the CERAD [49] and Braak and Braak criteria ([50]; Table 1). In all cases, the time between death and tissue processing was between 1.5 and 3 h. Upon removal, the brain tissue was immediately fixed in cold 4%

Table 1
Alzheimer's disease patients in the study

Patient	Age	Gender	NF/Aβ pathology Braak stage	Postmortem delay (h)	Cause of death
P1	80	Female	AD IV/B	2	-
P2	94	Female	AD V/C	1.5	Pulmonary tuberculosis
P7	91	Male	AD III/A and AGD	3	Hepatocarcinoma
P9	82	Male	AD V/C	3	Bronchopneumonia plus cardiac failure
P10	85	Male	AD V-VI/C	1.5	-

paraformaldehyde in phosphate buffer (PB: 0.1 M, pH 7.4), and after 12–24 h, the tissue was cut into small blocks and post-fixed in 2% paraformaldehyde and 2.5% glutaraldehyde in PB for 48–72 h at 4°C. Brain samples were obtained following the guidelines and approval of the Institutional Ethical Committee.

Tissue preparation

After fixation, the cortical tissue was washed in PB and sectioned in a vibratome (150 μm thickness). Selected sections were osmicated for 1 h at room temperature in PB containing 1% OsO_4, 7% glucose, and 0.02 M $CaCl_2$. After washing in PB, the sections were stained for 30 min with 1% uranyl acetate in 50% ethanol at 37ºC, and they were then dehydrated and flat embedded in Araldite [51]. The Araldite-embedded vibratome sections were then processed either for TEM or for FIB/SEM.

Transmission electron microscopy

Araldite-embedded vibratome sections were studied using a correlative light and EM method that has been previously described in detail elsewhere [51, 52]. Briefly, the vibratome sections were photographed under light microscope and then serially cut into semithin (2 μm thick) sections with a Leica EM UC6 ultramicrotome (Leica Microsystems, Wetzlar, Germany). The semithin sections were stained with 1% toluidine blue in 1% sodium borate, examined under the light microscope, and then photographed to locate the region of interest. Selected semithin sections were further sectioned into serial ultrathin sections (50–70 nm thick) with a diamond knife using a Leica ultramicrotome.

The ultrathin sections were collected on formvar-coated, single-slot nickel grids, and stained with uranyl acetate and lead citrate. Digital pictures were captured at different magnifications in a JEOL JEM-1011 (JEOL Ltd., Tokyo, Japan) electron microscope equipped with a digitalizing image system (SC1000 ORIUS, 11 megapixel; Gatan, Pleasanton, CA).

Dual beam electron microscopy (FIB/SEM)

Embedded vibratome sections were glued onto a blank Araldite block and trimmed. In order to select the region of interest, several semithin sections (1–2 μm of thickness) were obtained from the surface of the block and stained with toluidine blue as described above. The blocks containing the embedded tissue were then glued onto aluminum sample stubs using conductive carbon adhesive tabs (Electron Microscopy Sciences, Hatfield, PA). All the surfaces of the Araldite blocks, except for the surface to be studied (the top surface containing the sample), were covered with colloidal silver paint (Electron Microscopy Sciences, Hatfield, PA) to prevent charging artifacts. The stubs with the mounted blocks were then placed into a sputter coater (Emitech K575X, Quorum Emitech, Ashford, Kent, UK) and were coated with gold/palladium for 15 to 30 s to facilitate charge dissipation. The ultrastructural three-dimensional study of the samples was carried out using a dual beam microscope (Crossbeam® Neon40 EsB, Carl Zeiss NTS GmbH, Oberkochen, Germany). This instrument combines a high-resolution field-emission SEM column (Gemini® column, Carl Zeiss NTS GmbH, Oberkochen, Germany) with a focused gallium ion beam (FIB), which permits thin layers of material to be removed from the sample surface on a nanometer scale. As soon as one layer of material has been removed (or milled) by the FIB, the freshly exposed surface of the sample is imaged by the SEM using the backscattered electron detector. The sequential automated use of FIB milling and SEM imaging allowed us to obtain long series of photomicrographs that represent a three-dimensional sample of selected regions of the neuropil (see [47] for further information about the FIB/SEM methodology).

For this study, we obtained images of 2048 × 1536 pixels, at a resolution of 5.99 to 9.97 nm per pixel; each individual photomicrograph therefore covered a field of view that ranged from 12.27 × 9.20 to 20.42 × 15.31 μm^2. The layer of material milled by the FIB in each cycle (equivalent to section thickness) was 20 nm in all samples. The number of serial sections

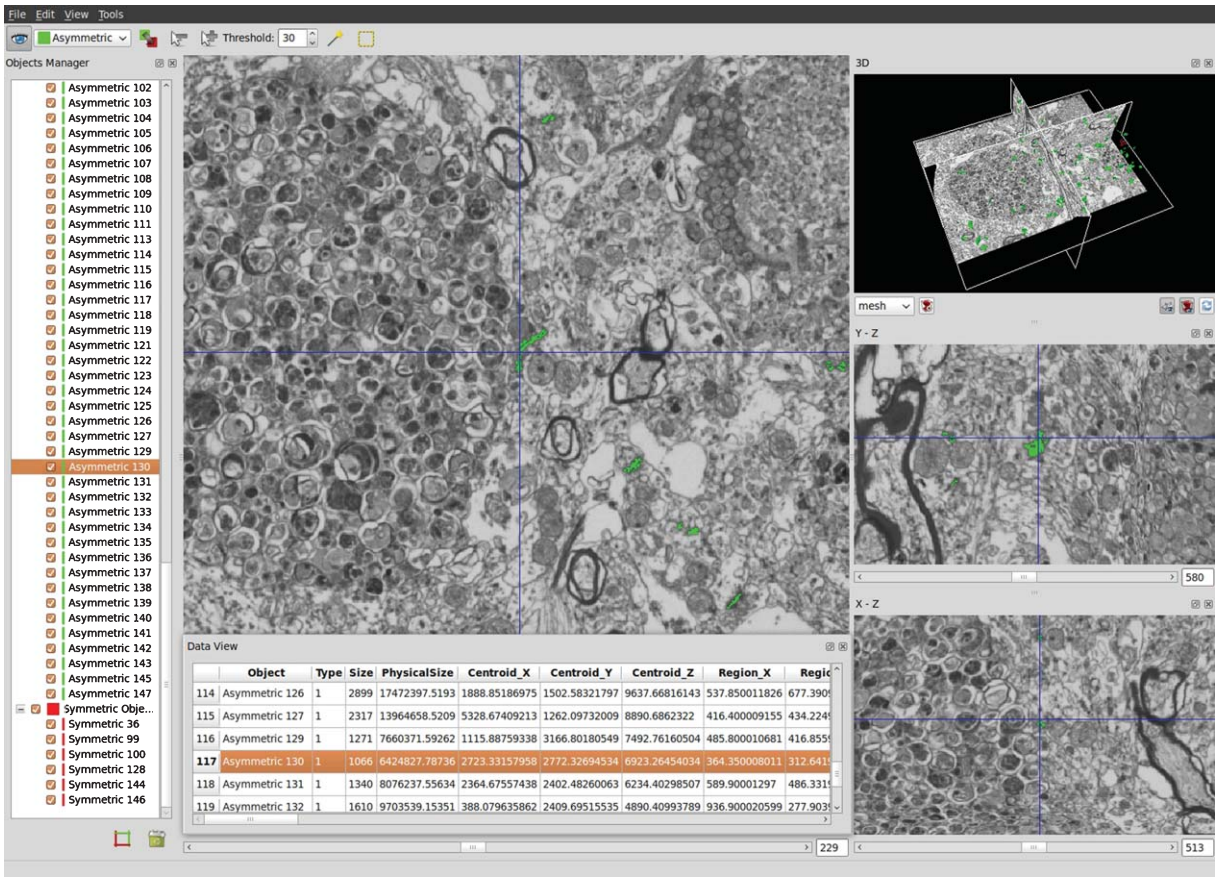

Fig. 1. Screenshot of Espina, the software tool used for the segmentation of synaptic junctions. In the central panel, one of the sections comprising the stack is shown with some synaptic junctions already segmented (green profiles). The segmented synaptic junctions can also be visualized in a 3D reconstruction of the tissue (upper right panel) or in orthogonal sections (right middle and right bottom panels). Every synaptic junction is color-coded (asymmetric synapses in green, symmetric synapses in red) and given a unique number, so they can be individually accessed using the left panel. Geometrical features of the reconstructed 3D objects such as their size and position are automatically calculated (bottom panel).

obtained for each sample varied between 135 and 625 (mean 349.25). The milling current of the FIB ranged from 500 pA to 1 nA and the SEM was set to 1.8 to 2.0 kV acceleration potential.

Alignment and visualization of serial images: Construction of the counting volume

Stacks of images were taken from the frontal cortex (Brodmann area 10). We analyzed plaques as well as neighboring areas (of the same layer and cortical area) that were devoid of dystrophic neurites and Aβ deposits. These neighboring areas were described as plaque-free regions (Supplementary Video 1; available online: http://www.j-alz.com/issues/34/vol34-4.html#supplementarydata04). Two different regions were examined within the plaques that were constituted either mainly by dystrophic neurites (Dn regions), with few or no Aβ deposits (Supplementary Video 2), or by both dystrophic neurites and large amounts of extracellular Aβ (Dn/Aβ regions) (Supplementary Video 3).

For the alignment (registration) of the stack of images we used Fiji (http://fiji.sc). We applied a rigid registration method (translation only, no rotation) to avoid any deformation of single sections. After registration, the resulting stack was filtered and resized. We used a Gaussian Blur filter with Fiji to eliminate noisy pixels. The images in the stack were then scaled to one half of their original size in order to save computer memory.

Reconstructing structures in the stacks of serial sections

Espina software was used for the automated segmentation and counting of synapses in the reconstructed 3D volume [48] (Fig. 1). In order to quantify the number of

objects per unit volume, a 3D unbiased counting frame must be constructed within the stack [53]. This 3D unbiased counting frame is a regular rectangular prism enclosed by three acceptance planes and three exclusion planes marking its boundaries. All objects within the counting brick or intersecting any of the acceptance planes are counted, while any object outside the counting brick or intersecting any of the exclusion planes is not [47].

Reconstruct Software 1.1.0.0 [54] was used to carry out the serial reconstruction of somata (neurons and glia), dystrophic neurites, and extracellular Aβ deposits. Each structure was assigned a different name and a color, and it was manually traced through the stacks of images. Once segmentation of these structures was performed, the generated meshes were exported to vrml format (Reconstruct) or to stl format (Espina). Each mesh was then loaded into the 3D modeling suite Blender 3D (http://www.blender.org). Blender makes it possible to configure each mesh and the entire scene easily in real-time. Inside this application each mesh surface is smoothed and its material properties (diffuse color, translucency, gloss) are defined. After each mesh is configured, the entire scene is composed, lights, camera, and camera animation are added, and some test renders are performed. When the test renders are satisfactory, the whole scene is exported via a python script to Yafaray native xml format (http://www.yafaray.org), which is an open-source hyper-realistic raytracer that allows us to get high-quality render frames that were used for composing each final video. In order to render each frame for each video, we used an SGI Prism multiprocessor with 16 Itanium processors and 32 GB of memory. Each frame took between 10 min and 1 h to be rendered. Finally, the video composition and encoding were performed in the sequence editor of Blender 3D (Supplementary Videos 4–6).

RESULTS

To better interpret the images obtained with FIB/SEM, we first examined the plaques using TEM in the same tissue. What follows is a brief description of the appearance of the plaques with these two methods.

Study of Aβ plaques using TEM microscopy

Types of Aβ plaques

As seen with TEM microscopy, Aβ plaques are formed by two major pathological components: Aβ fibrils or deposits and dystrophic neurites filled with different cytoplasmic inclusions and organelles. These elements, together with numerous apparently normal and altered neuronal and glial processes made up the plaques. However, as previously described (e.g., [22, 55–57]), different types of Aβ plaques were distinguished according to their appearance and composition. In general, two main types of plaques can be recognized: One type is characterized by a central core of densely packed Aβ fibrils ("Aβ-cored plaque") surrounded by a "white halo" containing dispersed fibrils of Aβ, glial processes, and dystrophic neurites (Fig. 2), where no or very few synapses are present (non-synaptic area) (see also [58, 59]). These Aβ-cored plaques may contain abundant (Fig. 2) or relatively few dystrophic neurites (Supplementary Figure 1). The other main type of plaques ("Aβ-diffuse plaques") are constituted by the same elements as Aβ-cored plaques, but Aβ is present as lax bundles, not forming a core, although arranged in a "plaque shape" (Supplementary Figures 2 and 3). These plaques are much less conspicuous at the EM level than Aβ-cored plaques. As occurs with Aβ-cored plaques, diffuse plaques may contain abundant dystrophic neurites (Supplementary Figure 3) or relatively few (Supplementary Figure 2).

Ultrastructure of dystrophic neurites

Dystrophic neurites show a variety of morphologies, with different sizes, cytoplasmic inclusions, and organelles (mitochondria, autophagosomes, lysosomes) (as can be seen in Fig. 3). Mitochondria were easily identified by the presence of inner and outer membranes surrounding an electrondense matrix containing mitochondrial crests. It was frequently observed that mitochondria in most dystrophic neurites exhibited morphological abnormalities (consistent with autophagic degradation; see [17, 60]), suggesting that they are metabolically compromised (see [45] and references contained therein).

As previously described in mice models of AD (e.g., [16, 45, 61]), the vacuolar structures of putative autophagic nature showed different morphologies and heterogeneous intraluminal contents, which suggests different degrees of alteration; from vacuoles with a multilamellar/densely compacted, amorphous content (Fig. 3A–C) to vacuoles containing an electrondense core formed by an amorphous non-lamellar material (Fig. 3D). Moreover, some dystrophic neurites show relatively few cytoplasmic inclusions and organelles (Fig. 3A) whereas others show a large number of these structures (Fig. 3B–D).

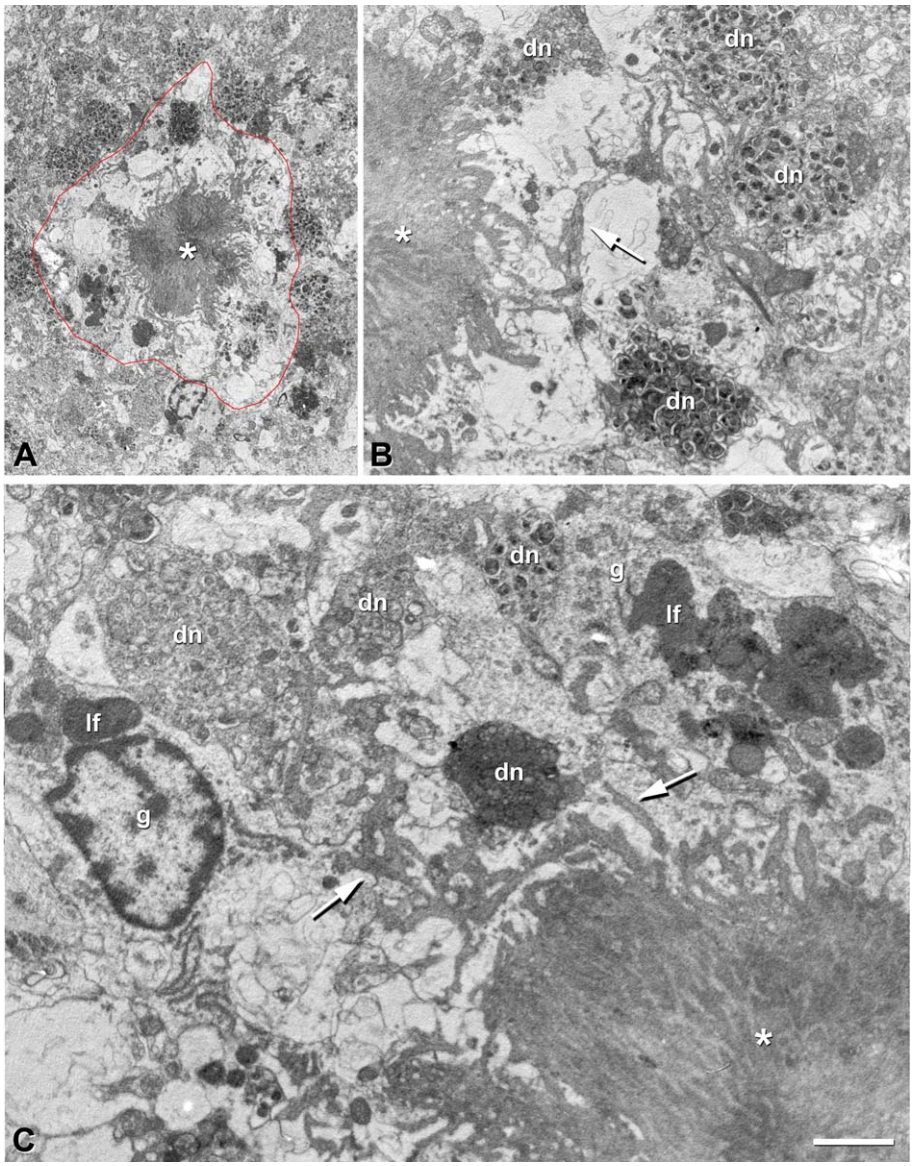

Fig. 2. Aβ-cored plaque in the frontal cortex (Brodmann area 10) from patient P2. A) Low-power TEM micrograph showing the Aβ core (asterisk) and the surrounding halo outlined with a red line, where no or very few synapses are present (non-synaptic area). B, C) Higher magnification of A, showing Aβ fibrils (arrows) emanating from the core, glial cells and their processes (g) and dystrophic neurites (dn). Granules or bodies of lipofucsin (lf) can also be identified. Scale bar (in C): A, 6.7 μm; B, 2.1 μm; C, 1.4 μm.

In addition, a filamentous material that resembles fibrillar Aβ aggregates of the plaques was commonly found within some dystrophic neurites that were located close to the Aβ core of the plaques (Supplementary Figure 4). Finally, within or near the plaques, there were axon terminals forming synapses, which appeared to represent early stages of axonal degeneration, since some of them contained vacuoles typical of well-developed dystrophic neurites or other abnormal disposition of axonal organelles although the pathological appearance was less obvious (Fig. 4).

Study of Aβ plaques using FIB/SEM

We compared the images obtained with TEM and FIB/SEM within different regions of the Aβ plaques. In order to facilitate the 3D reconstruction of the plaques, we first identified, by light microscope, the plaques

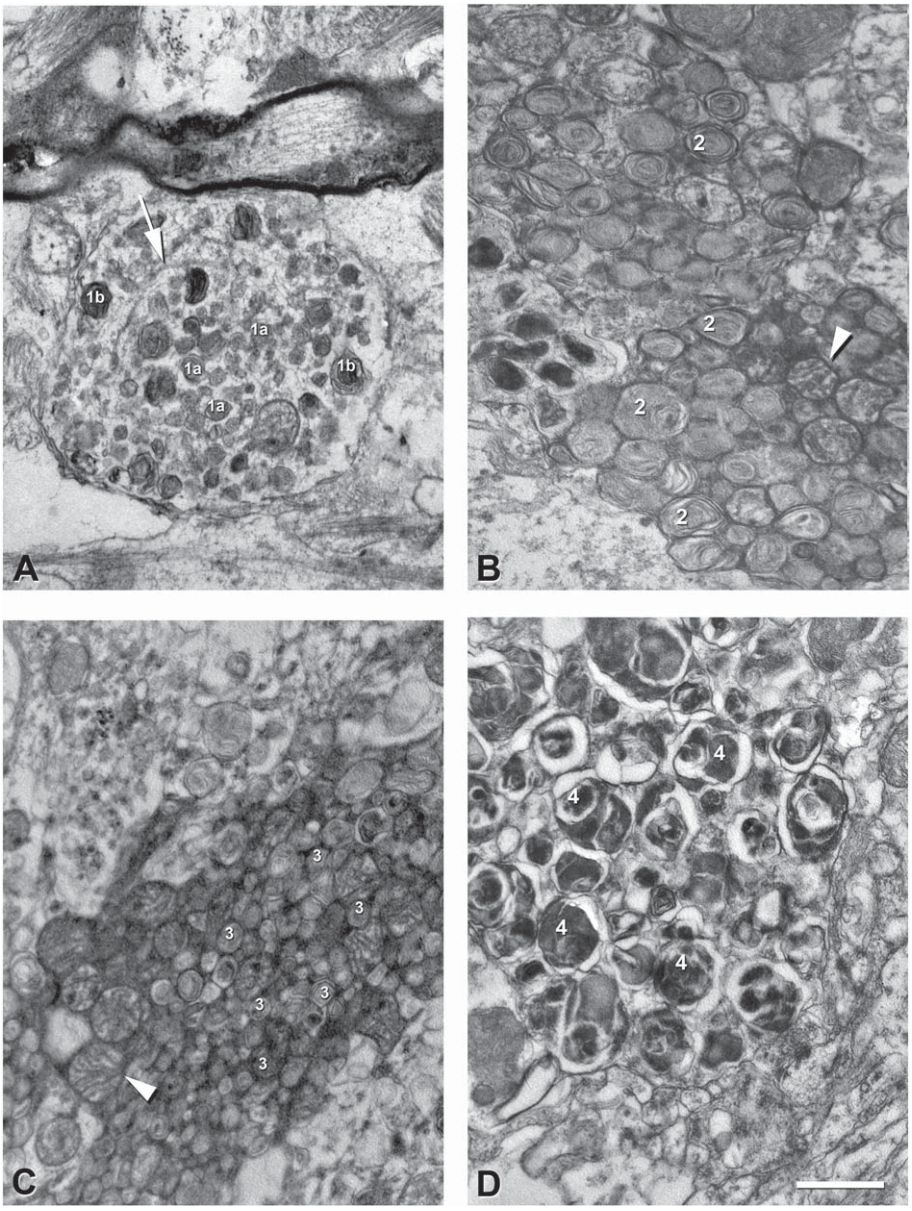

Fig. 3. TEM micrographs showing different types of dystrophic neurites in the frontal cortex (Brodmann area 10) of patients P9 (A) and P2 (B, C, D). A) The dystrophic neurite contains neurofilaments with a circular orientation (arrow) and small (1a) and large (1b) cytoplasmic vacuoles and organelles loosely distributed. The vacuole contents appeared dense, compacted, amorphous and multilamellar (especially, the largest ones, 1b). B) The dystrophic neurite is filled with large vacuoles with contents that appeared dense, compacted, amorphous and multilamellar (2). Some mitochondria with a normal appearance can be observed (arrowhead). C) The dystrophic neurite contains small dense bodies (3), similar in appearance to those in A (1a) but more closely packed. Some apparently normal mitochondria are observed (arrowhead). D) The dystrophic neurite shows large vacuoles containing an electrondense core formed by an amorphous non-lamellar material (4). Scale bar (in D): A–D, 0.6 μm.

in toluidine-blue stained plastic semithin sections that were taken from the surface of the block (Fig. 5A, B). Since the last semithin section obtained is adjacent to the surface of the remaining block, it was used as a guide for the subsequent study with the dual beam electron microscope. In order to select the regions of interest, the last semithin section obtained was compared with a SEM image of the tissue block and the appropriate regions were selected (see Fig. 5A, C). Thereafter, the region of interest was sequentially

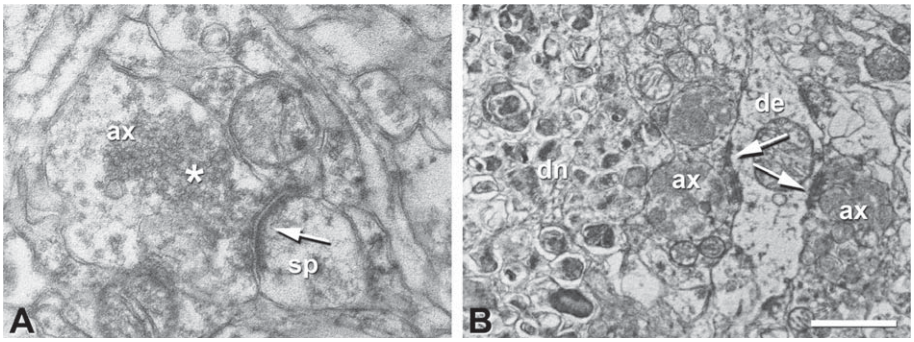

Fig. 4. TEM micrographs showing axon terminals forming synapses, which appear to represent early stages of axonal degeneration. These micrographs were taken near (A) or within (B) a plaque from the frontal cortex (Brodmann area 10) from patient P2. A, B) Abnormal-looking axon terminals (ax) forming synapses (arrows) with a dendritic spine (sp) and with a dendritic shaft (de), respectively. The asterisk in A indicates an abnormal-looking cluster of synaptic vesicles. Note in B that the axons (ax) contain vacuoles typical of dystrophic neurites (see Fig. 3). Dn, dystrophic neurite. Scale bar (in B): A, 0.5 μm; B, 0.8 μm.

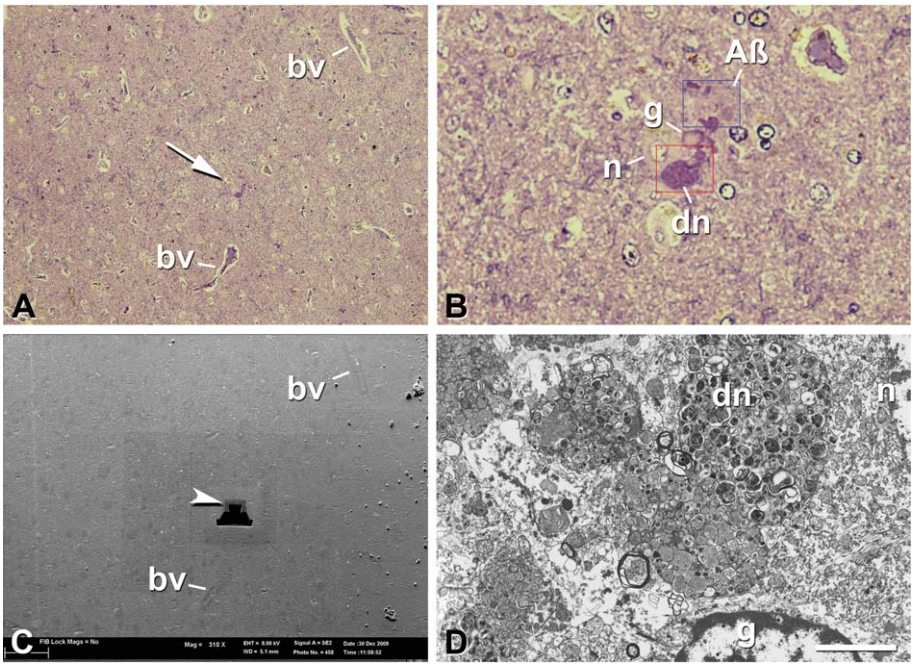

Fig. 5. Correlative light microscopy and FIB/SEM of a plaque located in layer IV of the frontal cortex of patient P2. A, B) Low- and high-magnification photomicrographs, respectively, of a toluidine blue-stained semithin section obtained from a tissue block that was later studied with the dual beam microscope. In A, a plaque (arrow) can be identified, and two blood vessels (bv) have been located as landmarks. In B, a higher magnification photomicrograph of the same plaque shows a dystrophic neurite (dn), a glial cell (g), a neuron (n), and an amyloid deposit (Aβ). The red and blue rectangles indicate the regions that were later imaged using FIB/SEM in the Dn and Dn/Aβ regions of the plaque, respectively. C) Low-magnification SEM micrograph of the surface of the block. Since the semithin section shown in A and the surface of the block are immediately adjacent, the same blood vessels (bv) can be identified and used as landmarks to locate the position of the plaque. A trench has already been milled with its frontal part (arrowhead) providing the series of images corresponding to the region inside the red rectangle in B. D) First microphotograph of the serial sections taken in the red square region shown in B, where portions of the same dystrophic neurite (dn), glial cell (g), and neuron (n) are shown. Note that the plane of section of the FIB is perpendicular to the plane of section of the semithin section shown in A and B. Scale bar (in D): A, C, 82 μm; B, 17.1 μm; D, 3.3 μm. See also Supplementary Videos 2 and 3.

milled and imaged as described in the Material and Methods section.

Reconstruction of the extracellular deposits of Aβ and dystrophic neurites

The availability of long series of consecutive sections facilitates the visualization and analysis of different elements in the neuropil. Indeed, neuronal and glial processes or individual mitochondria can be relatively easily followed in successive serial sections. These advantages are particularly important to study in detail the ultrastructural alterations that occur in AD, since it is possible to analyze all elements (normal and abnormal) present in the plaque and their 3D relationship (Fig. 6; Supplementary Videos 4–6).

Different types of dystrophic neurites could be reconstructed within the plaques (Fig. 6), as well as the extracellular Aβ, which in single sections did not seem to occupy a large area of the plaque (Fig. 6I–P). However, reconstructions revealed that the extracellular Aβ formed a continuous complex mesh (Fig. 6S). Many of the dystrophic neurites were found to be degenerating axons since in serial sections they were observed to make synaptic contacts with dendritic shafts and dendritic spines (Fig. 7). Interestingly, we observed that some dendritic elements established synapses with both dystrophic and non-dystrophic axons (Fig. 8).

Identification and counting of synapses: number of synapses per unit of volume

To test the validity of FIB/SEM for counting of synapses in the human cerebral cortex within and outside plaques, stacks of images were taken from different regions of the plaques and from regions with no pathological alterations (plaque-free regions) located in the same cortical areas and layers as the plaques under study. What follows is a detailed analysis of the plaque illustrated in Fig. 5 which was constituted by dystrophic neurites and deposits of Aβ not forming a central core. Supplementary Videos 2 and 3 show the stacks of images from two regions of the plaque illustrated in Fig. 5A, B, one constituted mainly by dystrophic neurites (Dn region) and with few or no Aβ (Supplementary Video 2; stack of 499 images) and a second region that was formed by both dystrophic neurites and large amounts of extracellular Aβ (Dn/Aβ region) (Supplementary Video 3; stack of 625 images). The images observed in these regions were compared with those obtained in an adjacent plaque-free region (Supplementary Video 1; stack of 352 images).

A structure was identified as a synapse when the following elements were clearly recognized: presence of densities on the cytoplasmic faces in the pre- and post-synaptic membranes (synaptic membrane densities); synaptic vesicles in the pre-synaptic axon terminal adjacent to the pre-synaptic density; and a synaptic cleft, although this last element may not be visible if sectioned obliquely or frontally (*en face*). Synapses were classified into asymmetric and symmetric synapses based on the prominent or thin post-synaptic density, respectively (reviewed in [62]). Since the synaptic junctions were fully reconstructed using FIB/SEM (Figs. 9 and 10), the classification of the vast majority of synapses as asymmetric or symmetric was possible [47]. Therefore, it was feasible to count the exact number and types of synapses within a three-dimensional unbiased counting brick.

In the examples illustrated in Figs. 9 and 10, which include plaque-free, Dn, and Dn/Aβ regions, the density of synapses was 263×10^6 mm^3 in the plaque-free region, whereas in the Dn and Dn/Aβ regions the density was 61×10^6 mm^3 and 44×10^6 mm^3, respectively. Thus, the density of synapses in the Dn and Dn/Aβ regions was about one fourth or less than in the plaque-free regions.

Synapse distribution: 3D spatial analysis

The position of every synapse is given by its center of gravity or centroid. The information about the position of synapses in three-dimensional space can be readily obtained from the Espina software, and can be subsequently analyzed by spatial statistical tools [63]. Points in space (the centroids of synaptic junctions in our case) can be distributed according to three basic patterns: regular, clustered, and random. In a regular or dispersed pattern, every point is located as far as possible from its neighbors, resulting in a lattice-like distribution of points with regular inter-point distances. In clustered patterns, the points tend to concentrate in groups, leaving other regions of space empty. Finally, in a random pattern (or homogeneous Poisson point process), the points are distributed in such a way that the position of any given point is independent from the position of any other point. That is, in a random distribution each point is equally likely to occur at any position and is not affected by the location of the other points. Although there are no clear-cut limits between these three distributions, the random pattern represents a boundary condition between dispersed and clustered spatial processes [64, 65]. We have used SA3D software [66] to calculate two commonly used functions to analyze the three-dimensional distribution of synapses in space, the G and F functions. To calculate the G function, the distance between each point in the sample

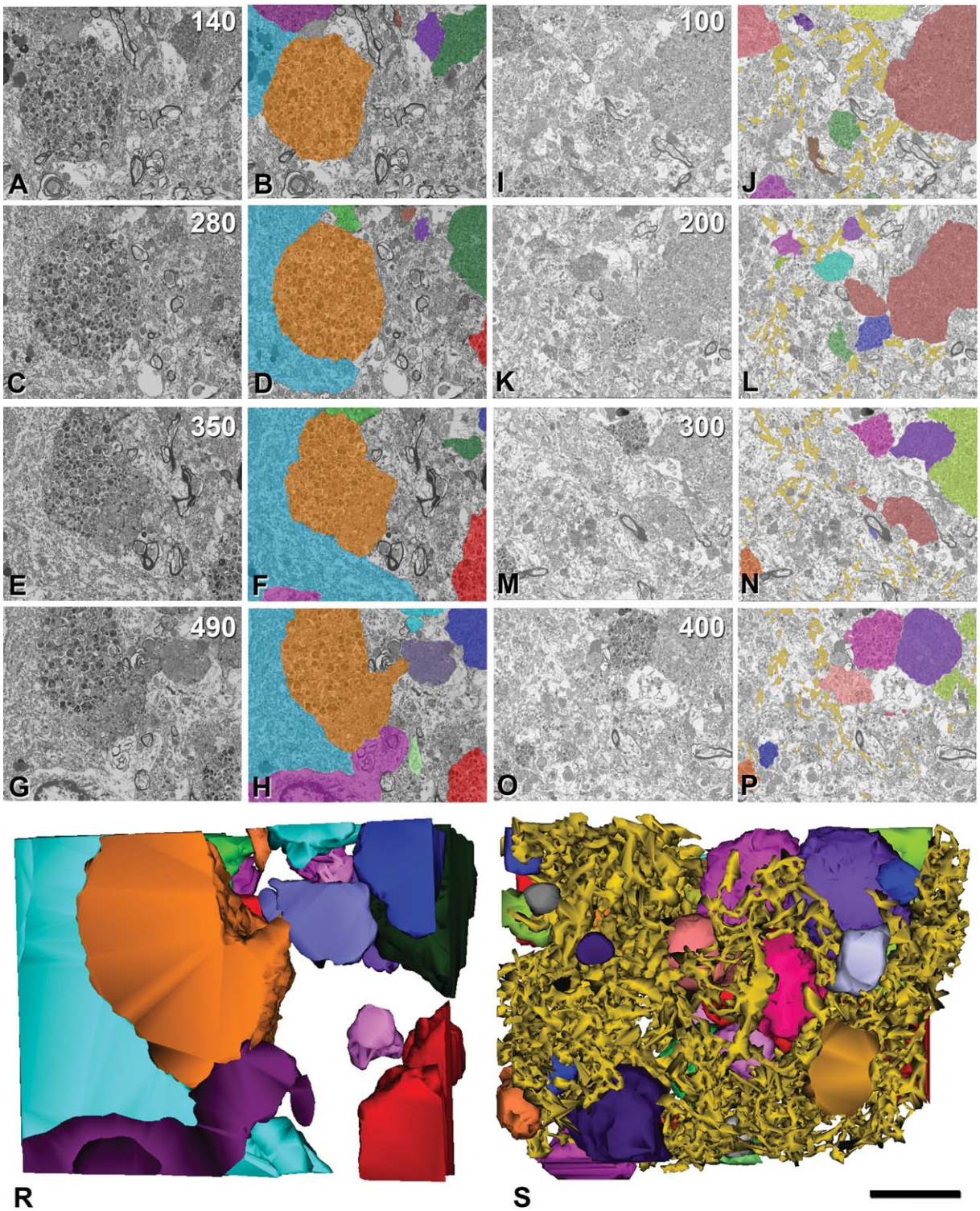

Fig. 6.

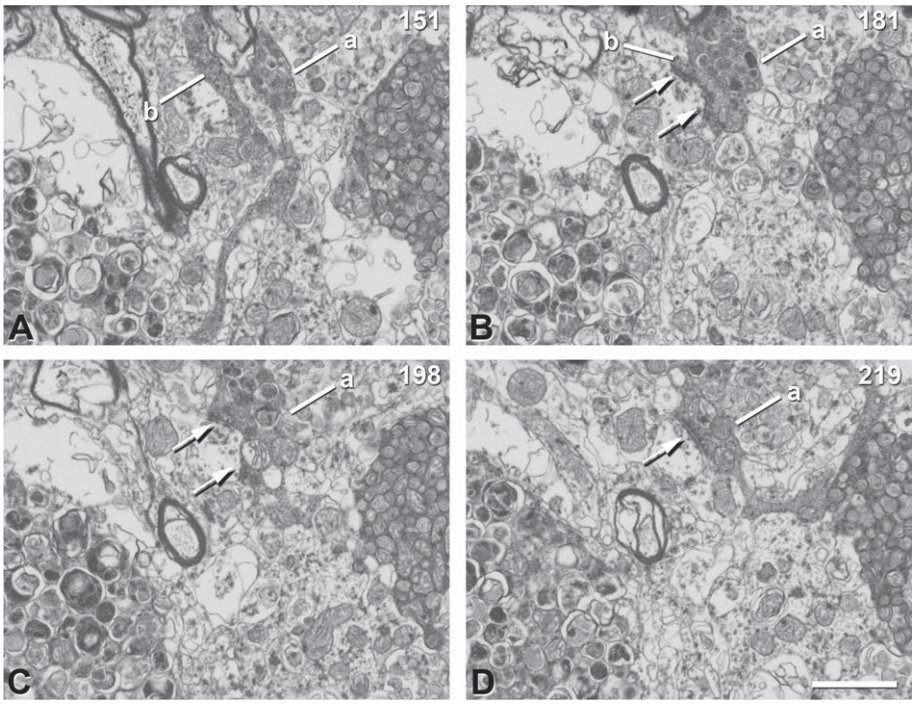

Fig. 7. Synaptic contacts established by two abnormal looking axonal processes (*a*, *b*) in the Dn region reconstructed with FIB/SEM. A–D) Illustrate sections 151, 181, 198 and 219, respectively (Supplementary Video 2). B) Shows that process *b* establishes an asymmetric synaptic contact (arrows) with a dendritic profile. Process *a* contains numerous dense cytoplasmic inclusions and organelles typical of dystrophic neurites. C, D) Show that process *a* establishes an asymmetric synaptic contact (arrows) with the same dendritic profile as *b* (see supplementary Video 2). Note that if only the single sections illustrated in B were available, it would appear that the synaptic contact was established by a single abnormal axon, since it is very difficult to distinguish that there are two processes (*a* and *b*). Scale bar (in D): A–D, 1.5 μm.

and its nearest neighbor is measured and the cumulative probability of having a nearest neighbor at a given distance or less is plotted. To estimate the F function, a regular grid is traced within the volume under study. The distances between each grid-crossing point and its nearest neighboring centroid are measured and the cumulative probability plotted as a function of distance. In a random pattern, the theoretical G and F functions take the same values (see [67], p. 101), so they can be represented by a single curve to be compared with the observed experimental values (Fig. 11). Our preliminary results indicate that in plaque-free regions the spatial distribution of synapses was nearly random since both the G and F functions closely resemble the theoretical curve that represents the G and F functions of a homogeneous Poisson process (Fig. 11). In Dn/Aβ and Dn regions of the plaques, however, the pattern was clearly clustered, as indicated by the fact that the G and F functions lay at the left and right side, respectively, of the theoretical curve corresponding to the theoretical Poisson process [67] (Fig. 11). More precisely, the G function increases rapidly because in a clustered pattern nearest neighbors are closer than would be expected in a random process. The F function rises more slowly because many centroids in the population are far from the grid-crossing points due to

Fig. 6. Methodology for reconstruction of structures visualized in FIB/SEM serial sections. A, C, E, G) Illustrate sections 140, 280, 350, 490 taken from the Dn region shown in Fig. 5B (red rectangle). B, D, F, H) Same images as in A, C, E, G, respectively, after pseudocoloring to label the different structures. I, K, M, O) Illustrate sections 100, 200, 300, 400 taken from the Dn/Aβ region shown in Fig. 5B (blue rectangle). J, L, N, P) Same images as in I, K, M, O respectively, after pseudocoloring. A given structure was followed in serial sections and was assigned the same color and name in the different sections. R, S) 3D reconstructions obtained with the Reconstruct software of the Dn and Dn/Aβ regions, respectively. In the Dn region, the soma of a neuron (light blue) and a glial cell (purple) and several dystrophic neurites (other colors) were reconstructed. In the Dn/Aβ region, the extracellular Aβ (yellow) and several dystrophic neurites (other colors) were reconstructed. These reconstructions were exported to the Blender software to generate Supplementary Videos 5 and 6, respectively. Note that all dystrophic neurites that were represented in different colors in the Reconstruct software were represented as brown elements in the videos whereas the color of the extracellular Aβ and of the neuronal and glial somata were maintained. Scale bar (in S): A–P, 7.2 μm; R, S, 4 μm.

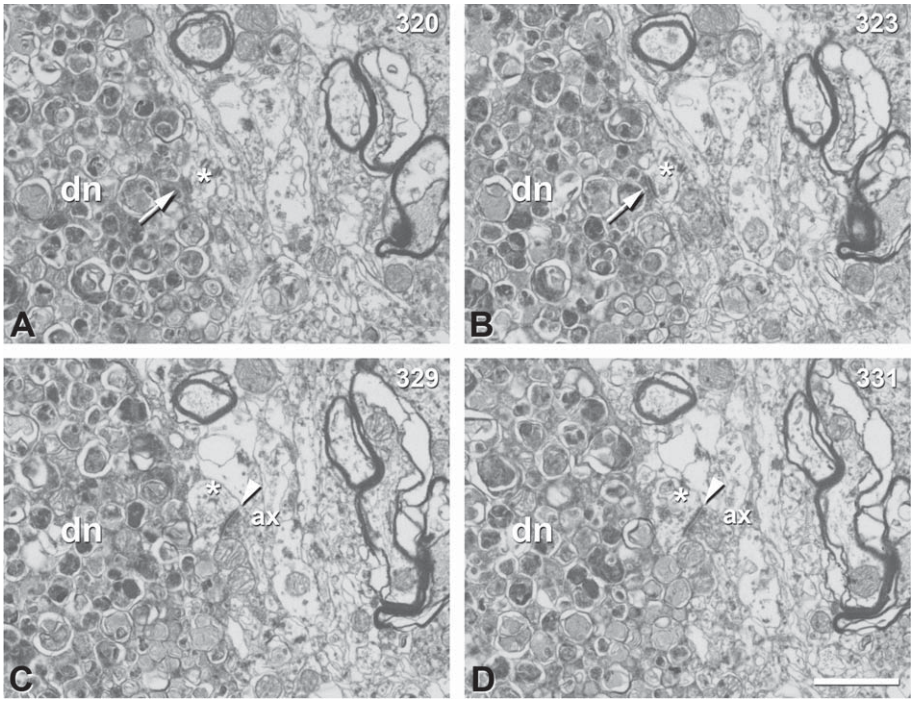

Fig. 8. Synaptic contact established by a dystrophic neurite in the Dn region reconstructed with FIB/SEM. A–D) Illustrate sections 320, 323, 329 and 331 (Supplementary Video 2). A synaptic contact (arrows in A and B) is established between a large dystrophic neurite (dn) (axon in this case that contains numerous dense bodies) and a dendritic profile indicated by an asterisk. The postsynaptic element also establishes a synapse with a normal axon (ax) (arrowhead in C–D). Scale bar (in D): 1.5 μm.

the presence of empty spaces. This clustered pattern is most probably due to the fact that synapses are lost in the space occupied by Aβ deposits and dystrophic neurites, so the remaining synapses apparently concentrate in the available space between these pathological structures.

DISCUSSION

In the present study we have shown that FIB/SEM is an excellent tool to study in detail the ultrastructure and alterations of the synaptic organization of the brain of AD patients in particular, and of the human brain in general. Since a number of studies have dealt with the ultrastructure of the cerebral cortex of AD patients from biopsy material, showing high quality images of the different components of the plaques (e.g., [14–26]), in the present study we focused mainly on the utility of FIB/SEM to study synaptic alterations in the cerebral cortex of AD patients. Using this technology it is possible to reconstruct different types of plaques and the surrounding neuropil to find new aspects of the pathological process associated with the disease, namely; to count the exact number and types of synapses in different regions of the plaques, to study the spatial distribution of synapses and to analyze the morphology and nature of the various types of dystrophic neurites.

Identification and counting of synapses

In the human brain tissue examined in the present study to test the validity of the application of FIB/SEM, it was possible to easily count both the total number and identify the types of synapses in different regions of the plaques. What follows is a brief discussion about the methods of counting synapses in comparison with FIB/SEM.

The number and density of synapses is one of the most commonly used measures in neurobiology to analyze different aspects of the organization of the brain both in health and disease, including brain complexity, learning, memory and plasticity, degree of alterations under pathological circumstances, etc. Therefore, a major aim of numerous researchers has been to find simple and accurate methods for estimating the number

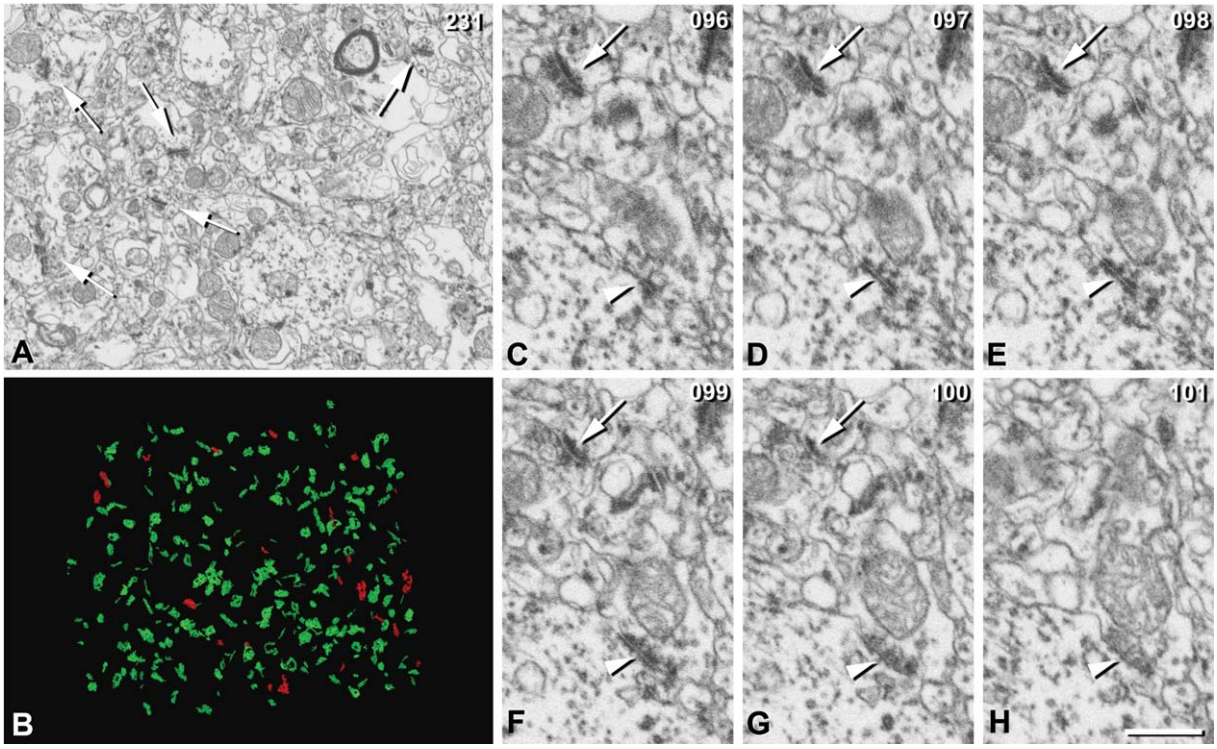

Fig. 9. FIB/SEM images obtained from the plaque-free region from the frontal cortex (Brodmann area 10) of patient P2. A stack of 351 serial images separated by 20 nm was obtained. A) Image 231 of the series (Supplementary Video 1) showing several synaptic contacts (arrows). B) Three-dimensional reconstruction of all the synaptic junctions present in the same stack of serial sections (Supplementary Video 4). Green and red objects represent asymmetric and symmetric synaptic profiles, respectively. C–H) Consecutive serial sections (096–101 of the stack of images) illustrating an asymmetric (arrows) and a symmetric synapse (arrowheads). Note the difference in the thickness of the post-synaptic densities between asymmetric (thick) and symmetric (thin) synapses. Scale bar (in F): A, 2 μm; B, 3.2 μm; C–H, 0.8 μm.

and density of synapses. The number of synapses has been estimated for surface areas and volumes using a variety of methods. Since these numbers depend on the size and shape of the synaptic junctions, and these may vary in different regions, at present the most common strategy is to estimate the number of synapses present in a unit volume using stereological methods. Thanks to these stereological methods it is possible to infer three-dimensional characteristics of synaptic junctions observed two-dimensionally, and to relate their sizes and numbers to a given volume of tissue (for a review, see [68]).

The identification of the morphological types of synapses is also critical from a functional point of view since the vast majority of axon terminals forming asymmetric synapses are excitatory (glutamatergic) and those forming symmetric synapses are inhibitory (GABAergic) [69]. Thus, changes in the density and in the proportion of asymmetric and symmetric synapses would represent modifications of the excitatory/inhibitory balance of the cortical circuits. The problem is that in single sections the synaptic cleft and the pre- and post-synaptic densities are often blurred if the plane of the section does not pass at right angles to the synaptic junction. In these cases, synapses cannot be classified (uncharacterized synapses), which represents a major limitation since around 40–60% of the synaptic profiles cannot be identified as asymmetric or symmetric from the analysis of single sections (reviewed in [13, 47]). Furthermore, in these circumstances, misinterpreting a non-synaptic profile (false synaptic contact) as a truly synaptic contact or *vice versa* is a frequent drawback. Thus, examination of the same section is necessary but viewed with various tilt angles using the goniometer stage of the EM (which can be applied within a short range of angles), or more precisely by the examination of serial sections to classify the actual number of the asymmetric and symmetric synapses. Since these methods are extremely time-consuming and difficult, one approach is to include uncharacterized synapses in the asymmetric and symmetric types, according to the proportional

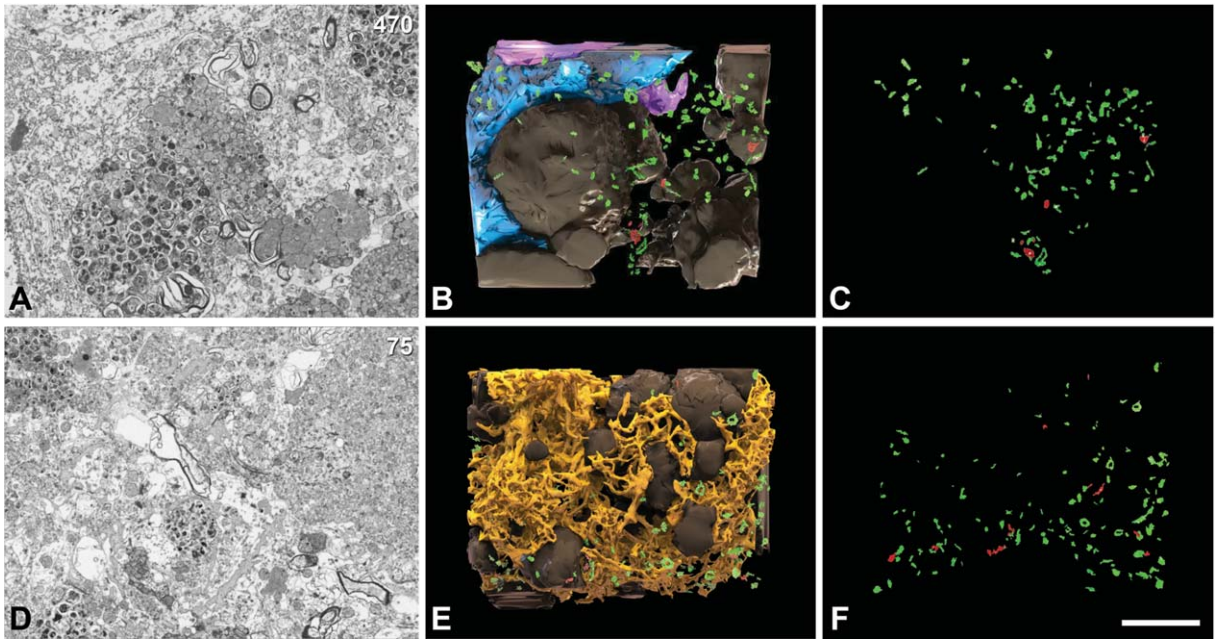

Fig. 10. Three-dimensional reconstructions of two stacks of serial sections obtained with the FIB/SEM from the Dn region (A–C) and the Dn/Aβ region (D–F) of a plaque from patient P2 (see Fig. 5). A) Low-power photomicrograph of section 470 of a stack of 499 serial sections from the Dn region showing several dystrophic neurites and synapses (Supplementary Video 2). B) Three-dimensional reconstruction of the same stack of the Dn region showing dystrophic neurites (brown), asymmetric synaptic junctions (green), symmetric synaptic junctions (red), a neuronal soma (blue) and a glial cell (purple) (Supplementary Video 5). In C, only synaptic profiles have been shown to reveal the absence of synapses in the regions occupied by dystrophic neurites and cell somata. D) Low-power photomicrograph of the Dn/Aβ region of a plaque showing image 75 of a stack of 625 serial sections. Dystrophic neurites, synaptic profiles and numerous Aβ fibrils can be identified (Supplementary Video 3). E) Three-dimensional reconstruction of the Dn/Aβ region showing the presence of several dystrophic neurites (brown) intermingled with numerous Aβ fibrils (yellow) (Supplementary Video 6). F shows only asymmetric (green) and symmetric (red) synapses occupying the available space among dystrophic neurites and Aβ fibrils. Scale bar (in F): A, D, 3.6 μm; B, C, E, F, 4.7 μm.

frequency of both types of synapses in each layer [70]. In this way, it is possible to obtain an estimate of the real ratio. However, using FIB/SEM the synaptic junctions are fully reconstructed, allowing the classification of practically all synapses as asymmetric or symmetric and resolving the cases of false synaptic contacts [47]. We concluded that FIB/SEM not only provides the actual number of synapses per volume but it is also much easier and faster to use than other currently available TEM methods. Furthermore, FIB/SEM is free of the errors introduced by stereological methods such as the misidentification of synapses and the under- or overestimation errors due to sampling. Finally, we confirmed in the present study that the resolution of the FIB/SEM micrographs was comparable to those obtained with the conventional TEM, but the quality was superior with FIB/SEM and the images were devoid of debris, folds, scratches and other artifacts that are commonly generated by TEM. Another advantage of FIB/SEM is that large samples up to a diameter of a 10 cm wafer, with a height up to 4 cm, can be loaded and they can be completely accessed, whereas for TEM the samples have to be trimmed to a small areal size before sectioning to obtain thin sections, with the consequent loss of a significant amount of material. Thus, with FIB/SEM technology a section comprising the whole hemisphere of a rat or a whole gyrus of the human brain can be sampled in many different locations and under different settings if needed without losing material, and this clearly represents a remarkable advantage. For example, in Fig. 5C, only a single FIB/SEM sample was taken, but tens of other samples could be obtained from the same region that is visible in the figure. In fact, the picture only shows a small portion of the actual tissue block, which is much bigger and could also be sampled. By contrast, for TEM the vibratome sections have to be trimmed to a relatively small block, losing a large portion of the material. Even using large single slot grids for TEM, the size of the slot is typically only 2×1 mm and the trimmed pyramid block used for EM is commonly much smaller.

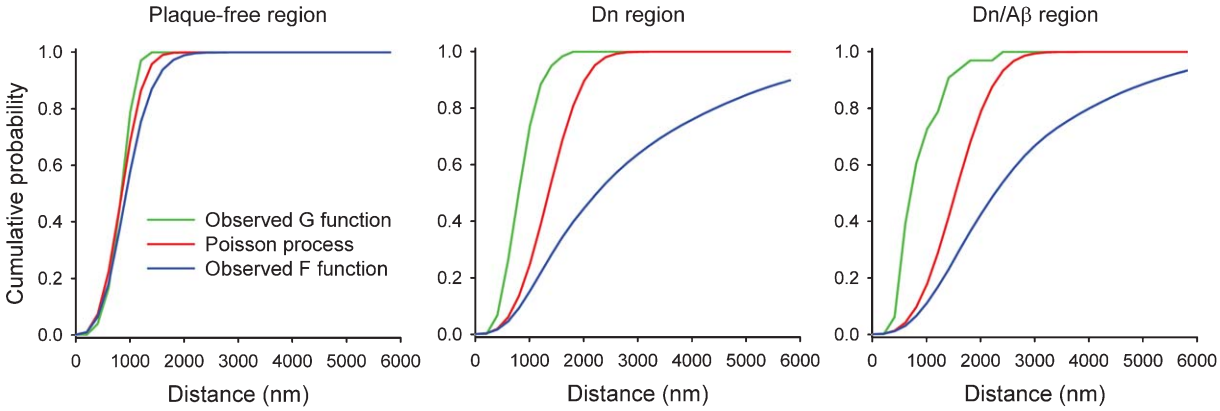

Fig. 11. Spatial analysis of three regions of cortical tissue from a patient of AD. Three regions of the neuropil have been analyzed from patient P2: plaque-free region, plaque region with dystrophic neurites (Dn) and plaque region with dystrophic neurites and Aβ deposits (Dn/Aβ). The G functions (green curves) and F functions (blue curves) have been estimated in each of these regions. The red curves represent the theoretical G and F functions that would be obtained from a random homogeneous Poisson process with the same density of points that were found in each region. Both theoretical functions are identical in these conditions so they are represented by a single curve in each region. Note that in the plaque-free region the experimentally observed G and F curves closely resemble the theoretical curve that would be expected for a Poisson process, indicating that synapses are distributed in a nearly random pattern. In Dn and Dn/Aβ regions of the plaque, however, G and F functions suggest a clustered pattern since i) the observed G functions are steeper (nearest neighbors are closer) than would be expected in a random pattern and ii) the observed F functions increase more slowly, since the distances between the grid points and the synapse centroids are larger than expected. This is due to the presence of empty spaces that are devoid of synapses since they are occupied by Aβ deposits or dystrophic neurites.

Dystrophic neurites

The ultrastructure of many of the dystrophic neurites studied in the present study was similar to those associated with Aβ plaques examined in animal models of AD and AD patients (e.g., [16, 25, 26]). We found that serial reconstructions of the dystrophic neurites revealed that many of them have an axonal origin, which is in line with studies in animal models (e.g., [61]). Interestingly, the synapses formed by these dystrophic axons could be with one or more postsynaptic dendrites (shafts or dendritic spines) and these postsynaptic dendrites also formed synapses with normal-looking axons. Thus, convergence of synaptic inputs from both abnormal and normal axons occurred in the dendrites adjacent to plaques.

Dystrophic neurites show a variety of morphologies, with different sizes and with different cytoplasmic inclusions and organelles (mitochondria, autophagosomes, lysosomes).

Types of Aβ plaques

The existence of different types of plaques with different degrees of alterations has prompted some researchers to propose that they represent different stages in the progression of the Aβ pathology. However, the morphologically heterogeneous pattern of Aβ plaques in different brain regions ([56, 71]; see also [72]) could also suggest that other region-specific factors contribute to this heterogeneity.

In this context, FIB/SEM can shed light on this hypothesis as 3D reconstructions of different types of plaques allow the examination in greater detail of all the elements within and near the different types of plaques. For example, as discussed above, thanks to the serial FIB/SEM reconstructions of dystrophic neurites, it was possible to discover that many dystrophic neurites established synapses with dendritic elements (see Figs. 7 and 8), indicating the axonal nature of these structures. This is in line with the alternative explanation for the existence of different types of plaques based on the anatomical connectivity of the cortical region, such that the location of neuritic plaques would depend on whether or not these regions receive input from axons of neurons bearing intracellular neurofibrillary tangles [56, 73, 74].

Loss of synapses and Aβ plaques

In the counting bricks examined here for counting the total number and types of synapses (illustrated in Figs. 9 and 10), we observed that in the Dn and Dn/Aβ regions there was a decrease of 77% and 83%,

respectively, in the number of synapses compared to the plaque-free region, whereas, the percentage of asymmetric and symmetric synapses was similar in the three regions (94% and 6% in the plaque-free region; 95% and 5% in the Dn region; and 91% and 9% in the Dn/Aβ region). Since the decrease of synapses affected both asymmetric and symmetric synapses and the majority of synapses are of the asymmetric type, it follows that a large part of this decrease was due to the loss of asymmetric synapses. In turn, it is well established that asymmetric synapses are formed mostly with dendritic spines. This therefore suggests that there would be a dendritic spine disconnection near the plaques. However, the quantitative data obtained here should be considered provisional, as more 3D reconstructions would need to be analyzed from additional plaques in different cortical layers and areas of different patients in order to obtain more solid quantitative data and conclusions.

Nevertheless, these findings fit very well with the extensive literature showing that plaques induce local alterations in the dendrites in contact with Aβ in both animal models [75–82] and AD patients (Merino-Serrais et al., unpublished data; Benavides-Piccione et al., unpublished data). These alterations include loss and morphological alterations of dendritic spines and the thinning of dendritic shafts in contact or passing through Aβ plaques. Therefore, it is most likely that the large decrease of synapses within and in the periphery of the plaques observed in the present study would correlate with a loss of dendritic spines. Interestingly, in a previous study we found that neurons in contact with Aβ plaques appeared to be normal at the ultrastructural level although the membrane of the neuronal somata in contact with the Aβ plaque lacked GABAergic axosomatic synapses in both the PP/PS1 mouse and in AD patients [83].

In addition, the portion of the soma of these neurons that was not in contact with the Aβ plaques established typical synapses, whereas synapses were absent from the region in direct contact with the Aβ plaques. In the present study, we have verified this observation by the partial reconstruction of the cell body of a pyramidal neuron (see Supplementary Video 2). Thus, direct contact of the Aβ plaque with the cell body does not induce perisomatic disconnection further away from the contact domain. Based on these findings, we propose that dendrites are more susceptible to the toxic effect of Aβ than the cell body. Thus, it is possible that the loss of dendritic spines is due to a toxic effect of Aβ on dendritic spines and consequently the loss of synapses. However, we cannot rule out the possibility that Aβ induces loss of synaptic axon terminals that form synapses with dendritic spines, with the consequent disappearance of these non-synaptic spines. Alternatively, both mechanisms may coexist. In this respect, although the Dn/Aβ region showed the lower density of synapses (44×10^6 mm^3 versus 263×10^6 mm^3 and 61×10^6 mm^3, in the plaque-free and Dn regions, respectively), the density of synapses was relatively high in spite of the presence of a large amount of Aβ forming a mesh-like structure in the neuropil. Further studies would be necessary to resolve this issue. Finally, it should be emphasized that counting the number of synapses is a simplistic way to try to correlate alterations of cortical circuits in AD since some of the synapses are formed by abnormal-looking axons that should also be taken into account in terms of their percentage and distribution.

In conclusion, although the quantitative results presented in this article are provisional, we show that FIB/SEM in combination with tools for the automated segmentation and counting of synapses in large stacks of EM images, such as the Espina software [48], represent new technologies that can be applied not only to the study of the AD brain, but also to the human brain in general. These developments allow huge advances in obtaining large amounts of data on the synaptic densities and distributions that otherwise would be very difficult, if not impossible, to perform with other available techniques to examine the human brain.

ACKNOWLEDGMENTS

The authors are grateful to Virginia García Marín for her help in the early stage of this study and Lorena Valdés for technical assistance. This work was supported by grants from the following entities: CIBERNED (CB06/05/0066), Fundación CIEN (Financiación de Proyectos de Investigación de Enfermedad de Alzheimer y enfermedades relacionadas 2008), Fundación Caixa (BM05-47-0), the Spanish Ministerio de Ciencia e Innovación (SAF2009-09394) and the Cajal Blue Brain Project, Spanish partner of the Blue Brain Project initiative from EPFL.

Authors' disclosures available online (http://www.j-alz.com/disclosures/view.php?id=1620).

REFERENCES

[1] Jucker M, Beyreuther K, Haass C, Nitsch R, Christen Y (2006) *Alzheimer: 100 Years and Beyond*, Springer-Verlag, Berlin Heidelberg.

[2] Hsieh H, Boehm J, Sato C, Iwatsubo T, Tomita T, Sisodia S, Malinow R (2006) AMPAR removal underlies Abeta-induced synaptic depression and dendritic spine loss. *Neuron* **52**, 831-843.

[3] Shankar GM, Li S, Mehta TH, Garcia-Munoz A, Shepardson NE, Smith I, Brett FM, Farrell MA, Rowan MJ, Lemere CA, Regan CM, Walsh DM, Sabatini BL, Selkoe DJ (2008) Amyloid-beta protein dimers isolated directly from Alzheimer's brains impair synaptic plasticity and memory. *Nat Med* **14**, 837-842.

[4] Snyder EM, Nong Y, Almeida CG, Paul S, Moran T, Choi EY, Nairn AC, Salter MW, Lombroso PJ, Gouras GK, Greengard P (2005) Regulation of NMDA receptor trafficking by amyloid-beta. *Nat Neurosci* **8**, 1051-1058.

[5] Spires-Jones TL, Meyer-Luehmann M, Osetek JD, Jones PB, Stern EA, Bacskai BJ, Hyman BT (2007) Impaired spine stability underlies plaque-related spine loss in an Alzheimer's disease mouse model. *Am J Pathol* **171**, 1304-1311.

[6] Arendt T (2009) Synaptic degeneration in Alzheimer's disease. *Acta Neuropathol* **118**, 167-179.

[7] Coleman P, Federoff H, Kurlan R (2004) A focus on the synapse for neuroprotection in Alzheimer disease and other dementias. *Neurology* **63**, 1155-1162.

[8] Dickson DW, Crystal HA, Bevona C, Honer W, Vincent I, Davies P (1995) Correlations of synaptic and pathological markers with cognition of the elderly. *Neurobiol Aging* **16**, 285-298; discussion 298-304.

[9] Masliah E, Mallory M, Alford M, DeTeresa R, Hansen LA, McKeel DW, Jr., Morris JC (2001) Altered expression of synaptic proteins occurs early during progression of Alzheimer's disease. *Neurology* **56**, 127-129.

[10] Selkoe DJ (2002) Alzheimer's disease is a synaptic failure. *Science* **298**, 789-791.

[11] Sze CI, Troncoso JC, Kawas C, Mouton P, Price DL, Martin LJ (1997) Loss of the presynaptic vesicle protein synaptophysin in hippocampus correlates with cognitive decline in Alzheimer disease. *J Neuropathol Exp Neurol* **56**, 933-944.

[12] Terry RD, Masliah E, Salmon DP, Butters N, DeTeresa R, Hill R, Hansen LA, Katzman R (1991) Physical basis of cognitive alterations in Alzheimer's disease: Synapse loss is the major correlate of cognitive impairment. *Ann Neurol* **30**, 572-580.

[13] DeFelipe J, Marco P, Busturia I, Merchan-Perez A (1999) Estimation of the number of synapses in the cerebral cortex: Methodological considerations. *Cereb Cortex* **9**, 722-732.

[14] DeKosky ST, Scheff SW (1990) Synapse loss in frontal cortex biopsies in Alzheimer's disease: Correlation with cognitive severity. *Ann Neurol* **27**, 457-464.

[15] Gonatas NK, Anderson W, Evangelista I (1967) The contribution of altered synapses in the senile plaque: An electron microscopic study in Alzheimer's dementia. *J Neuropathol Exp Neurol* **26**, 25-39.

[16] Masliah E, Sisk A, Mallory M, Mucke L, Schenk D, Games D (1996) Comparison of neurodegenerative pathology in transgenic mice overexpressing V717F beta-amyloid precursor protein and Alzheimer's disease. *J Neurosci* **16**, 5795-5811.

[17] Nixon RA, Wegiel J, Kumar A, Yu WH, Peterhoff C, Cataldo A, Cuervo AM (2005) Extensive involvement of autophagy in Alzheimer disease: An immuno-electron microscopy study. *J Neuropathol Exp Neurol* **64**, 113-122.

[18] Terry RD, Gonatas NK, Weiss M (1964) Ultrastructural studies in Alzheimer's presenile dementia. *Am J Pathol* **44**, 269-297.

[19] Luse SA, Smith KR, Jr. (1964) The ultrastructure of senile plaques. *Am J Pathol* **44**, 553-563.

[20] Masliah E, Hansen L, Albright T, Mallory M, Terry RD (1991) Immunoelectron microscopic study of synaptic pathology in Alzheimer's disease. *Acta Neuropathol* **81**, 428-433.

[21] Masliah E, Hansen L, Mallory M, Albright T, Terry RD (1991) Abnormal brain spectrin immunoreactivity in sprouting neurons in Alzheimer disease. *Neurosci Lett* **129**, 1-5.

[22] Masliah E, Mallory M, Deerinck T, DeTeresa R, Lamont S, Miller A, Terry RD, Carragher B, Ellisman M (1993) Re-evaluation of the structural organization of neuritic plaques in Alzheimer's disease. *J Neuropathol Exp Neurol* **52**, 619-632.

[23] Davies CA, Mann DM, Sumpter PQ, Yates PO (1987) A quantitative morphometric analysis of the neuronal and synaptic content of the frontal and temporal cortex in patients with Alzheimer's disease. *J Neurol Sci* **78**, 151-164.

[24] DeKosky ST, Scheff SW, Styren SD (1996) Structural correlates of cognition in dementia: Quantification and assessment of synapse change. *Neurodegeneration* **5**, 417-421.

[25] Praprotnik D, Smith MA, Richey PL, Vinters HV, Perry G (1996) Filament heterogeneity within the dystrophic neurites of senile plaques suggests blockage of fast axonal transport in Alzheimer's disease. *Acta Neuropathol* **91**, 226-235.

[26] Praprotnik D, Smith MA, Richey PL, Vinters HV, Perry G (1996) Plasma membrane fragility in dystrophic neurites in senile plaques of Alzheimer's disease: An index of oxidative stress. *Acta Neuropathol* **91**, 1-5.

[27] Alonso-Nanclares L, Gonzalez-Soriano J, Rodriguez JR, DeFelipe J (2008) Gender differences in human cortical synaptic density. *Proc Natl Acad Sci U S A* **105**, 14615-14619.

[28] Alonso-Nanclares L, Kastanauskaite A, Rodriguez JR, Gonzalez-Soriano J, DeFelipe J (2011) A stereological study of synapse number in the epileptic human hippocampus. *Front Neuroanat* **5**, 8.

[29] Kastanauskaite A, Alonso-Nanclares L, Blazquez-Llorca L, Pastor J, Sola RG, DeFelipe J (2009) Alterations of the microvascular network in sclerotic hippocampi from patients with epilepsy. *J Neuropathol Exp Neurol* **68**, 939-950.

[30] Gibson PH (1983) EM study of the numbers of cortical synapses in the brains of ageing people and people with Alzheimer-type dementia. *Acta Neuropathol* **62**, 127-133.

[31] Scheff SW, Price DA, Schmitt FA, Scheff MA, Mufson EJ (2011) Synaptic loss in the inferior temporal gyrus in mild cognitive impairment and Alzheimer's disease. *J Alzheimers Dis* **24**, 547-557.

[32] Scheff SW, Price DA, Schmitt FA, DeKosky ST, Mufson EJ (2007) Synaptic alterations in CA1 in mild Alzheimer disease and mild cognitive impairment. *Neurology* **68**, 1501-1508.

[33] Scheff SW, Price DA, Schmitt FA, Mufson EJ (2006) Hippocampal synaptic loss in early Alzheimer's disease and mild cognitive impairment. *Neurobiol Aging* **27**, 1372-1384.

[34] Scheff SW, Sparks DL, Price DA (1996) Quantitative assessment of synaptic density in the outer molecular layer of the hippocampal dentate gyrus in Alzheimer's disease. *Dementia* **7**, 226-232.

[35] Scheff SW, Sparks L, Price DA (1993) Quantitative assessment of synaptic density in the entorhinal cortex in Alzheimer's disease. *Ann Neurol* **34**, 356-361.

[36] Baloyannis SJ, Mauroudis I, Manolides SL, Manolides LS (2009) Synaptic alterations in the medial geniculate bodies and the inferior colliculi in Alzheimer's disease: A Golgi and electron microscope study. *Acta Otolaryngol* **129**, 416-418.

[37] Masliah E, Terry RD, Alford M, DeTeresa R (1990) Quantitative immunohistochemistry of synaptophysin in human neocortex: An alternative method to estimate density of presynaptic terminals in paraffin sections. *J Histochem Cytochem* **38**, 837-844.

[38] Masliah E, Terry RD, DeTeresa RM, Hansen LA (1989) Immunohistochemical quantification of the synapse-related protein synaptophysin in Alzheimer disease. *Neurosci Lett* **103**, 234-239.
[39] Honer WG, Dickson DW, Gleeson J, Davies P (1992) Regional synaptic pathology in Alzheimer's disease. *Neurobiol Aging* **13**, 375-382.
[40] Gabriel SM, Haroutunian V, Powchik P, Honer WG, Davidson M, Davies P, Davis KL (1997) Increased concentrations of presynaptic proteins in the cingulate cortex of subjects with schizophrenia. *Arch Gen Psychiatry* **54**, 559-566.
[41] Porter LL, White EL (1986) Synaptic connections of callosal projection neurons in the vibrissal region of mouse primary motor cortex: An electron microscopic/horseradish peroxidase study. *J Comp Neurol* **248**, 573-587.
[42] Stevens JK, Davis TL, Friedman N, Sterling P (1980) A systematic approach to reconstructing microcircuitry by electron microscopy of serial sections. *Brain Res* **2**, 265-293.
[43] Stalder M, Deller T, Staufenbiel M, Jucker M (2001) 3D-Reconstruction of microglia and amyloid in APP23 transgenic mice: No evidence of intracellular amyloid. *Neurobiol Aging* **22**, 427-434.
[44] Nuntagij P, Oddo S, LaFerla FM, Kotchabhakdi N, Ottersen OP, Torp R (2009) Amyloid deposits show complexity and intimate spatial relationship with dendrosomatic plasma membranes: An electron microscopic 3D reconstruction analysis in 3xTg-AD mice and aged canines. *J Alzheimers Dis* **16**, 315-323.
[45] Fiala JC, Feinberg M, Peters A, Barbas H (2007) Mitochondrial degeneration in dystrophic neurites of senile plaques may lead to extracellular deposition of fine filaments. *Brain Struct Funct* **212**, 195-207.
[46] DeFelipe J (2010) From the connectome to the synaptome: An epic love story. *Science* **330**, 1198-1201.
[47] Merchan-Perez A, Rodriguez JR, Alonso-Nanclares L, Schertel A, DeFelipe J (2009) Counting synapses using FIB/SEM microscopy: A true revolution for ultrastructural volume reconstruction. *Front Neuroanat* **3**, 18.
[48] Morales J, Alonso-Nanclares L, Rodriguez JR, DeFelipe J, Rodriguez A, Merchan-Perez A (2011) Espina: A tool for the automated segmentation and counting of synapses in large stacks of electron microscopy images. *Front Neuroanat* **5**, 18.
[49] Mirra SS, Heyman A, McKeel D, Sumi SM, Crain BJ, Brownlee LM, Vogel FS, Hughes JP, van Belle G, Berg L (1991) The Consortium to Establish a Registry for Alzheimer's Disease (CERAD). Part II. Standardization of the neuropathologic assessment of Alzheimer's disease. *Neurology* **41**, 479-486.
[50] Braak H, Braak E (1991) Neuropathological stageing of Alzheimer-related changes. *Acta Neuropathol* **82**, 239-259.
[51] DeFelipe J, Fairen A (1993) A simple and reliable method for correlative light and electron microscopic studies. *J Histochem Cytochem* **41**, 769-772.
[52] DeFelipe J, Fairen A (1982) A type of basket cell in superficial layers of the cat visual cortex. A Golgi-electron microscope study. *Brain Res* **244**, 9-16.
[53] Howard CV, Reed MG (2005) Unbiased Stereology, Garland Science/Bios Scientific Publishers, Oxon.
[54] Fiala JC (2005) Reconstruct: A free editor for serial section microscopy. *J Microsc* **218**, 52-61.
[55] Delaere P, Duyckaerts C, He Y, Piette F, Hauw JJ (1991) Subtypes and differential laminar distributions of beta A4 deposits in Alzheimer's disease: Relationship with the intellectual status of 26 cases. *Acta Neuropathol* **81**, 328-335.
[56] Thal DR, Rub U, Schultz C, Sassin I, Ghebremedhin E, Del Tredici K, Braak E, Braak H (2000) Sequence of Abeta-protein deposition in the human medial temporal lobe. *J Neuropathol Exp Neurol* **59**, 733-748.
[57] Wisniewski HM, Wen GY, Kim KS (1989) Comparison of four staining methods on the detection of neuritic plaques. *Acta Neuropathol* **78**, 22-27.
[58] Kidd M (1964) Alzheimer's disease–an electron microscopical study. *Brain* **87**, 307-320.
[59] Krigman MR, Feldman RG, Bensch K (1965) Alzheimer's presenile dementia. A histochemical and electron microscopic study. *Lab Invest* **14**, 381-396.
[60] Hariri M, Millane G, Guimond MP, Guay G, Dennis JW, Nabi IR (2000) Biogenesis of multilamellar bodies via autophagy. *Mol Biol Cell* **11**, 255-268.
[61] Sanchez-Varo R, Trujillo-Estrada L, Sanchez-Mejias E, Torres M, Baglietto-Vargas D, Moreno-Gonzalez I, De Castro V, Jimenez S, Ruano D, Vizuete M, Davila JC, Garcia-Verdugo JM, Jimenez AJ, Vitorica J, Gutierrez A (2012) Abnormal accumulation of autophagic vesicles correlates with axonal and synaptic pathology in young Alzheimer's mice hippocampus. *Acta Neuropathol* **123**, 53-70.
[62] Peters A, Palay SL (1996) The morphology of synapses. *J Nueurocytol* **25**, 687-700.
[63] Merchan-Perez A, Rodriguez JR, Gonzalez S, Robles V, DeFelipe J, Larrañaga P, Concha Bielza C (2013) Three-dimensional spatial distribution of synapses in the neocortex: A dual-beam electron microscopy study. *Cereb Cortex* (in press).
[64] Gaetan C, Guyon X (2009) *Spatial Statistics and Modeling*. Springer, Heidelberg.
[65] Illian J, Penttinen A, Stroyan H, Stroyan D (2008) *Statistical Analysis and Modelling of Spatial Point Patterns*. John Wiley & Sons Ltd., Hoboken, NJ.
[66] Eglen SJ, Lofgreen DD, Raven MA, Reese BE (2008) Analysis of spatial relationships in three dimensions: Tools for the study of nerve cell patterning. *BMC Neurosci* **9**, 68.
[67] O'Sullivan D, Unwin D (2002) *Geographic Information Analysis*. Wiley, Hoboken, NJ.
[68] Mayhew TM (1996) How to count synapses unbiasedly and efficiently at the ultrastructural level: Proposal for a standard sampling and counting protocol. *J Neurocytol* **25**, 793-804.
[69] Ascoli GA, Alonso-Nanclares L, Anderson SA, Barrionuevo G, Benavides-Piccione R, Burkhalter A, Buzsaki G, Cauli B, DeFelipe J, Fairen A, Feldmeyer D, Fishell G, Fregnac Y, Freund TF, Gardner D, Gardner EP, Goldberg JH, Helmstaedter M, Hestrin S, Karube F, Kisvarday ZF, Lambolez B, Lewis DA, Marin O, Markram H, Munoz A, Packer A, Petersen CC, Rockland KS, Rossier J, Rudy B, Somogyi P, Staiger JF, Tamas G, Thomson AM, Toledo-Rodriguez M, Wang Y, West DC, Yuste R (2008) Petilla terminology: Nomenclature of features of GABAergic interneurons of the cerebral cortex. *Nat Rev Neurosci* **9**, 557-568.
[70] DeFelipe J, Alonso-Nanclares L, Arellano JI (2002) Microstructure of the neocortex: Comparative aspects. *J Neurocytol* **31**, 299-316.
[71] Duyckaerts C, Delatour B, Potier MC (2009) Classification and basic pathology of Alzheimer disease. *Acta Neuropathol* **118**, 5-36.
[72] Blazquez-Llorca L, Garcia-Marin V, DeFelipe J (2010) Pericellular innervation of neurons expressing abnormally hyperphosphorylated tau in the hippocampal formation of Alzheimer's disease patients. *Front Neuroanat* **4**, 20.
[73] Thal DR, Glas A, Schneider W, Schober R (1997) Differential pattern of beta-amyloid, amyloid precursor protein and

apolipoprotein E expression in cortical senile plaques. *Acta Neuropathol* **94**, 255-265.

[74] Yilmazer-Hanke DM, Hanke J (1999) Progression of Alzheimer-related neuritic plaque pathology in the entorhinal region, perirhinal cortex and hippocampal formation. *Dement Geriatr Cogn Disord* **10**, 70-76.

[75] Bittner T, Fuhrmann M, Burgold S, Ochs SM, Hoffmann N, Mitteregger G, Kretzschmar H, LaFerla FM, Herms J (2010) Multiple events lead to dendritic spine loss in triple transgenic Alzheimer's disease mice. *PLoS One* **5**, e15477.

[76] Dong H, Martin MV, Chambers S, Csernansky JG (2007) Spatial relationship between synapse loss and beta-amyloid deposition in Tg2576 mice. *J Comp Neurol* **500**, 311-321.

[77] Knafo S, Alonso-Nanclares L, Gonzalez-Soriano J, Merino-Serrais P, Fernaud-Espinosa I, Ferrer I, DeFelipe J (2009) Widespread changes in dendritic spines in a model of Alzheimer's disease. *Cereb Cortex* **19**, 586-592.

[78] Knafo S, Venero C, Merino-Serrais P, Fernaud-Espinosa I, Gonzalez-Soriano J, Ferrer I, Santpere G, DeFelipe J (2009) Morphological alterations to neurons of the amygdala and impaired fear conditioning in a transgenic mouse model of Alzheimer's disease. *J Pathol* **219**, 41-51.

[79] Koffie RM, Meyer-Luehmann M, Hashimoto T, Adams KW, Mielke ML, Garcia-Alloza M, Micheva KD, Smith SJ, Kim ML, Lee VM, Hyman BT, Spires-Jones TL (2009) Oligomeric amyloid beta associates with postsynaptic densities and correlates with excitatory synapse loss near senile plaques. *Proc Natl Acad Sci U S A* **106**, 4012-4017.

[80] Merino-Serrais P, Knafo S, Alonso-Nanclares L, Fernaud-Espinosa I, DeFelipe J (2011) Layer-specific alterations to CA1 dendritic spines in a mouse model of Alzheimer's disease. *Hippocampus* **21**, 1037-1044.

[81] Spires TL, Meyer-Luehmann M, Stern EA, McLean PJ, Skoch J, Nguyen PT, Bacskai BJ, Hyman BT (2005) Dendritic spine abnormalities in amyloid precursor protein transgenic mice demonstrated by gene transfer and intravital multiphoton microscopy. *J Neurosci* **25**, 7278-7287.

[82] Tsai J, Grutzendler J, Duff K, Gan WB (2004) Fibrillar amyloid deposition leads to local synaptic abnormalities and breakage of neuronal branches. *Nat Neurosci* **7**, 1181-1183.

[83] Garcia-Marin V, Blazquez-Llorca L, Rodriguez JR, Boluda S, Muntane G, Ferrer I, DeFelipe J (2009) Diminished perisomatic GABAergic terminals on cortical neurons adjacent to amyloid plaques. *Front Neuroanat* **3**, 28.